Spatial distribution of reference evapotranspiration considering topography in the Taoer river basin of Northeast China

LiQiao Liang, LiJuan Li and Qiang Liu

ABSTRACT

Spatial distribution of reference evapotranspiration (ET_0) is essential in water resources planning and management, especially in semi-arid areas. In this paper, a digital elevation model is used in an 'interpolate-then-calculate' approach to calculating the spatially distributed ET_0 using the physically based Penman–Monteith equation in the Taoer river basin in China. The results show the following. (1) Of 11 interpolation methods, the Inverse Distance Weighting (IDW) method was found to be best for interpolating wind speed and a tri-variate secondary trend surface method was found most suitable for interpolating mean air temperature and relative humidity. Spatial modelling of the radiation environment considered the effects of elevation, slope and aspect. (2) Monthly values in January for the three meteorological variables showed larger spatial variations than in July, and just the reverse of net surface radiation. (3) The resulting ET_0 calculated at each grid cell with 200 m resolution and its spatial variation showed strong seasonal variation. Lower ET_0 was found in high-elevation southern Great Xingan mountains in the northwest basin, while higher values were located in the plains adjacent to the lower reach. (4) The ET_0 distribution by the 'interpolate-then-calculate' approach better reflected the effects of topography than that of the 'calculate-then-interpolate' approach.

Key words | interpolate-then-calculate, Penman–Monteith equation, reference evapotranspiration, spatial distribution, Taoer river basin, topographic influences

LiQiao Liang
LiJuan Li (corresponding author)
Institute of Geographic Sciences and Natural
    Resources Research,
Chinese Academy of Sciences,
11A Datun Road, Chaoyang District,
Beijing 100101,
China
E-mail: lilj@igsnrr.ac.cn

Qiang Liu
School of Environment, Beijing Normal University,
Beijing 100875,
China

INTRODUCTION

Evapotranspiration is one of the most important variables to reflect the combined effects of climate change and catchment characteristics, which impact on the water cycle in the basin scale (Blackie & Simpson 1993; Xu et al. 2006). Exploration of the spatial distribution of ET can provide valuable information for water resources planning and management in catchments, especially in arid and semi-arid areas.

Furthermore, many hydrological, agricultural and environmental models have been developed and widely used, including assessments of global water cycle intensification due to climate change (Huntington 2006) and frameworks to predict impact of re-vegetation activities on regional hydrology (Zhang et al. 2001; Donohue et al. 2007). The implementation of these models requires a spatially distributed measure of potential evapotranspiration (McVicar et al. 2007).

In order to avoid ambiguities that existed in the definition of potential evapotranspiration, the reference evapotranspiration concept was introduced by irrigation engineers and researchers in the late 1970s and the early 1980s (Allen et al. 1998). Reference evapotranspiration (ET_0) is defined as 'the rate of evapotranspiration from a hypothetical reference with an assumed crop height of 0.12 m, a fixed surface resistance of $70\,\mathrm{s\,m^{-1}}$ and an albedo of 0.23, closely resembling the evapotranspiration from an

extensive surface of green grass of uniform height, actively growing, well-watered and completely shading the ground'. The only factors affecting ET_0 are climate parameters. Consequently, ET_0 is a climatic parameter and can be computed from weather data. Various calculation methods have been performed to estimate ET_0 from different climatic variables for different locations (DehghaniSanij *et al.* 2004; Utset *et al.* 2004; Joshua *et al.* 2005; Liu & Lin 2005; Dinpashoh 2006).

Reference evapotranspiration by many methods are mostly calculated for individual point locations. Many researchers interpolated station values to obtain a spatial distribution of ET_0 using isoline or grid automatic drawing software (Dalezios *et al.* 2002; Dinpashoh 2006). This distribution cannot provide more precise spatial variation, although it may show spatial characteristics of ET_0 to some extent. Xu *et al.* (2006) spatially distributed ET_0 for the entire Changjiang (Yangze) river basin with an approximate 25 km resolution output. Zhang & Shen (2007) spatially distributed Penman–Monteith ET_0 with Surfer8.0 software using data for 616 meteorological stations in China.

The above-mentioned research mainly used interpolation methods dominated by the point measurements and were performed by the 'calculate-then-interpolate' approach. Topographic influences on climate variables (Yoshino 1975; Daly 2006; Stahl *et al.* 2006) were not considered in these approaches, even although the study areas have complex terrain and large elevation ranges. The method of calculating ET_0 then spatially interpolating it geometrically in two dimensions (longitude and latitude) implies that topographic changes of key meteorological variables between stations are not considered in the implementation.

Zhao *et al.* (2004) spatially distributed ET_0 in the Chinese Loess Plateau using the improved Hargreaves method; the results showed the importance of topographic influence on air temperature and resulting ET_0. However, their results did not consider the influence of topography on other meteorological variables affecting ET_0. McVicar *et al.* (2007) spatially distributed physically realistic expressions of ET_0 (Penman–Monteith equation) by ANUSPLIN software, considering topographic influences on forcing variables in the Coarse Sandy Hilly Catchments in the Yellow river basin in China. They filled the niche of spatially distributing ET_0 (a physically based ET_0 formulation) while modelling the influence of topography and land-surface conditions on the forcing meteorological variables by using an 'interpolate-then-calculate' approach.

ANUSPLIN provides interpolation of noisy multivariate data using thin plate-smoothing splines by providing comprehensive statistical analyses, data diagnostics and spatially distributed standard errors (Hutchinson 2004). Additionally, the software has been used extensively for spatially interpolating hydrometeorological surfaces including air temperature (McVicar & Jupp 2002; Yan *et al.* 2005), precipitation (McVicar *et al.* 2002), wind speed (Hutchinson *et al.* 1984), pan evaporation (Jeffrey *et al.* 2001), solar radiation (Jeffrey *et al.* 2001; McVicar & Jupp 2002), and vapour pressure (Jeffrey *et al.* 2001; McVicar & Jupp 2002). However, its high cost is the major drawback of applying commercial ANUSPLIN software in developing countries. In China, its application is restricted to researchers cooperating with Australian researchers.

The objective of our study is to spatially interpolate ET_0 using an 'interpolate-then-calculate' approach, reflecting topographic influences in ArcGIS software with a long-term dataset from 1961 to 2005. First, appropriate interpolation methods were selected to spatially distribute key meteorological variables (e.g. wind speed, air temperature and relative humidity). Second, the net radiation environment was spatially modelled. Third, using grid maps of meteorological variables thus obtained, ET_0 was spatially calculated by the physically based Penman–Monteith equation.

STUDY AREA AND DATA DESCRIPTION

Study area

The Taoer river basin (45°6′–47°12′N, 117°18′–124°6′E) is located in Northeast China (Figure 1) with an area of about $42 \times 10^3 \, km^2$, supporting a population of 3.6 million. From west to east, the basin changes from the upper reach to the lower reach, with topography changing from mountain to hill to plain and climate from semi-humid to semi-arid. The highest elevation difference exceeds 1,500 m.

Soil transits reveal forest soil to chernozem to chestnut soil, mixed with other types such as meadow soil, saline soil,
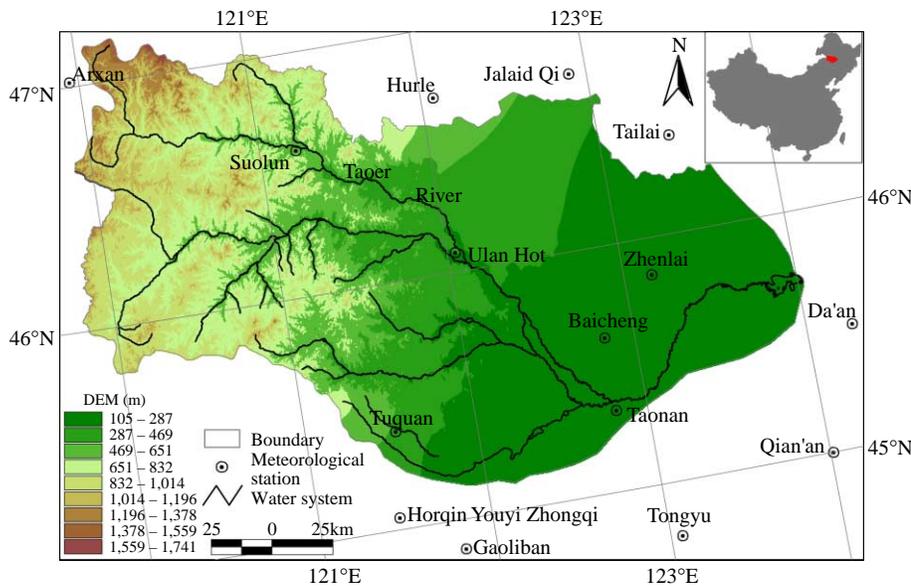
Figure 1 | The inset map shows the location of the Taoer river basin (red area) in China. The main map shows the Taoer river basin and its digital elevation model. Meteorological stations and water system are shown by encircled dots and black lines, respectively.

aeolian sandy soil and swamp soil. Landscape transits reveal 'priority to forests' to 'priority to stock raising', then 'priority to agriculture in agri-pastoral transitional zone'. In the lower reach, lakes and marsh developed because the river bed swung frequently.

Mean annual precipitation is 390 mm, while pan evaporation is about 1,800 mm which is four times higher than precipitation. Moreover, monthly and inter-annual variation of precipitation is large. The highest annual precipitation during 1961–2001 is almost four times the lowest precipitation. Growing season precipitation accounts for 89.0% of annual precipitation. As an important part of the Northeast China Plain, the Taoer river basin is one of the most important agricultural regions in China.

Under the combined impact of global climate change and intensified human perturbations, land use and land coverage has changed and the effects of desertification and salinization are evident. On the other hand, the decrease of wetland areas and the deterioration of the regional water environment are prominent and several rivers have become seasonal. The alkali-saline land in the east of the Taoer river basin is one of the most severe in China. The area of the alkali-saline land reached $15.3 \times 10^3 \, \text{km}^2$ in 1999, accounting for 36.4% of the Taoer river basin (Liang *et al.* 2008). In recent decades, high evapotranspiration has intensified

the salinization. The percentage of severe alkali-saline land to the total alkali-saline land area increased from 26.9% in 1958 to 43.7% in 1999 (Zhang & Wang 2002). The area of secondary salinization land in 2000 was reported to be 10 times that of the value in 1950 (Jiang 2007). Generally, the middle and lower reaches of the Taoer River are environmentally fragile (Zhao 1999) with ecosystems sensitive to climate change (Gao *et al.* 2000).

Data description

Monthly meteorological data were obtained from 15 stations in and around the Taoer river basin for this study from January 1961 through December 2005. Four monthly meteorological variables were recorded including: (1) mean air temperature (T, °C); (2) mean wind speed (u, m s^{-1}); (3) mean relative humidity (RH, %); (4) bright sunshine hours (n, hours). The historical dataset is 45 years long implying that it is representative, stable and comparable and that it describes temporal and spatial distribution of climate. All variables were averaged over the recent 45 years for each month at each station to represent the long-term climate in the Taoer river basin. Data were provided by China Meteorological Administration (CMA), Jilin Meteorological Bureau and Inner Mongolia Meteorological Bureau.
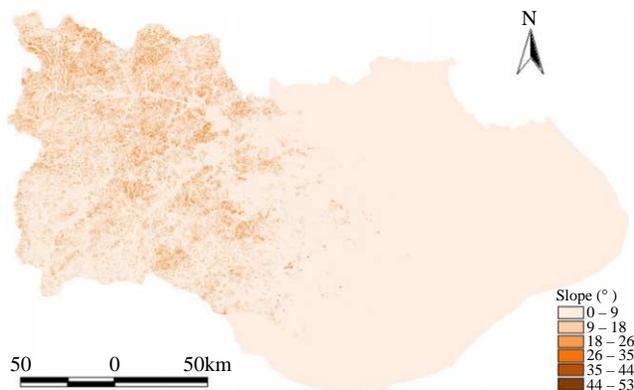
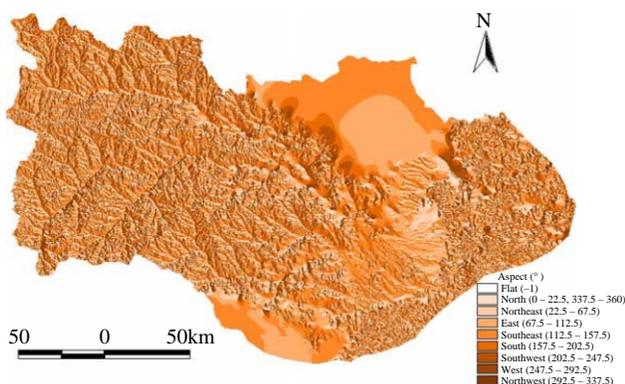**Figure 2** │ Slope map of the Taoer river basin derived from the DEM.

The wind speed measurements at 10 m height above the ground were transformed to wind speed at 2 m height by the wind profile relationship introduced in Food and Agriculture Organization (FAO) paper 56 (Allen *et al.* 1998). The formula is

$$u_2 = u_z \frac{4.87}{\ln(67.8z - 5.42)} \tag{1}$$

where z is 10 m.

A digital elevation model (DEM) with grid resolution of 30 m × 30 m for the Taoer river basin was selected (Figure 1). The slope map (Figure 2) and aspect map (Figure 3) were derived from the DEM using Arcview 3.2 software.

In order to provide a brief overview of the climate of the study area, meteorological data measured at 15 stations were spatially averaged to provide regional values. Monthly data were subsequently temporally averaged from 1961 to 2005. The Taoer river basin climate is characterized by:

Figure 3 │ Aspect map of the Taoer river basin derived from the DEM.

(1) T peaks in July (Figure 4(a)); (2) Figure 4(b) shows a bimodal mode in the monthly distribution of u with a strong peak in April and a weaker peak in late autumn; (3) maximum n occurs in May (Figure 4(c)) which is governed by the day length and modulated by increasing cloud cover associated with the summer monsoons; and (4) similar variations occur in RH seasonal cycle with the minimum in April and maximum in July (Figure 4(d)). The general pattern of RH is governed by the summer monsoons. The similar variations of monthly main meteorological variables were also reported for other areas in China (Xu *et al.* 2006; McVicar *et al.* 2007).
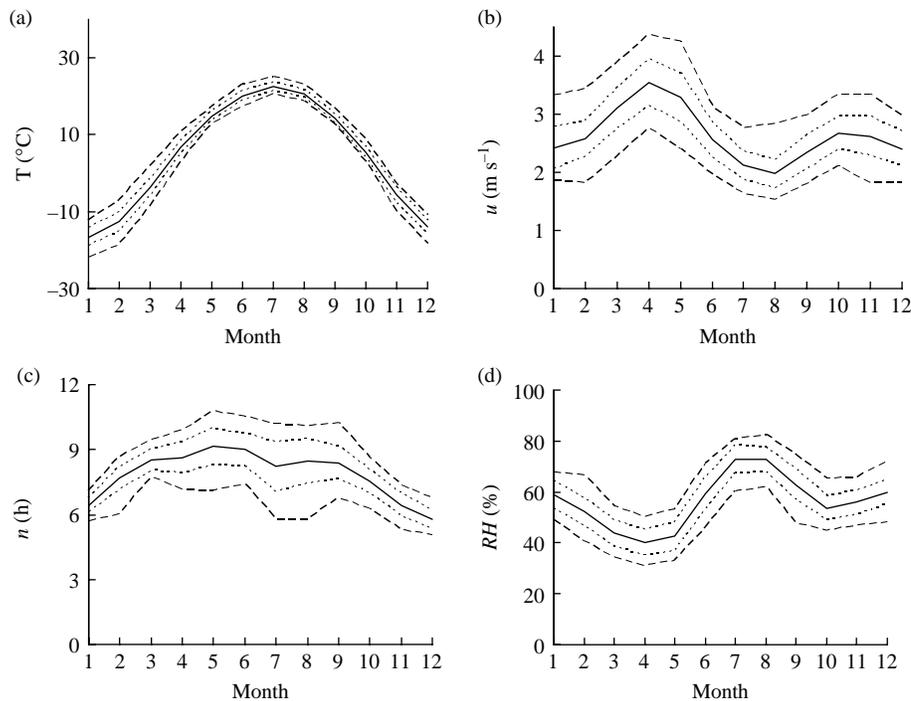
METHODS

Spatially interpolating the required meteorological variables

To spatially distribute ET_0 on a grid-cell requires that the input variables were either spatially interpolated or spatially modelled. There are many algorithms available to spatially interpolate meteorological data sets: (1) IDW (Franke 1982; Watson & Philip 1985; Marquínez *et al.* 2003); (2) various forms of kriging (Dalezios *et al.* 2002); (3) spline (Price *et al.* 2000); and (4) trend surface (Vicente-Serrano *et al.* 2003). These methods can be performed using commercial GIS software; however, they only take latitude and longitude into account and neglect elevation.

Common methods which consider topography to interpolate meteorological data include tri-variate splines in ANUSPLIN (McVicar *et al.* 2007), cokriging (Krajewski 1987; Yates & Warwick 1987) and tri-variate trend surface (Yu *et al.* 2004). These methods require special software (e.g. Australian ANUSPLIN software with the core of tri-variate splines). Furthermore, additional meteorological variables are needed for interpolation (although this method is not widely applied). Presently, climate researchers use the tri-variate trend surface which also reflects the influence of topography on spatial distribution of meteorological variables.

In this study, 11 commonly used interpolation methods were compared and tested for their interpolation quality in relation to wind peed, relative humidity and air temperature

Figure 4 | Monthly values of: (a) T (°C); (b) u (m s^{-1}); (c) n (hours); (d) RH (%). The mean during the period 1961–2005 (solid line), $\pm$ 1 standard deviation (dot lines), and the minimum and maximum (dash lines) are shown.

(Table 1). The best methods were identified and selected for further testing on monthly interpolation of the above three meteorological variables. The correlation coefficients between the interpolated values of ET$_0$ and the original values for the four best methods are shown in Table 1.

The tri-variate secondary trend surface method was used in this study to interpolate mean monthly relative humidity and air temperature for the 15 stations into a grid of 200 m × 200 m in latitude and longitude since it reflects the effects of topography and also has the highest correlation coefficient. To interpolate wind speed, the IDW method was used in this study since it demonstrated the highest correlation coefficient (although the tri-variate secondary trend surface method considers the DEM).

All interpolation was performed at 200 m resolution, which is higher than the 25 km resolution used in Xu *et al.*'s (2006) study.

The basic function for tri-variate trend surface is:

$$Y = F(\lambda, \varphi, h) + \varepsilon \qquad (2)$$

where Y is the predicted meteorological value; $F(\lambda, \varphi, h)$ is the macroscopic distribution function and generally expressed by tri-variate trend surface or quadratic polynomial regression equation; λ, φ and h are longitude, latitude and elevation respectively; ε is the error term generated by microtopography and random error (which can be neglected if microtopography is not considered).

Table 1 | Comparison of interpolation quality of tri-variate secondary trend surface, IDW, kriging (linear) and kriging (exponential) (values in this table are mean correlation coefficients of 12 months from the cross-validation tests)

	Tri-variate secondary trend surface	IDW	Kriging (linear)	Kriging (expotential)
Wind speed	0.72	0.78	0.76	0.75
Relative humidity	0.88	0.80	0.85	0.84
Air temperature	0.92	0.84	0.89	0.87

The function for tri-variate secondary trend surface is:

$$Y = b_0 + b_1\lambda + b_2\varphi + b_3h + b_4\lambda\varphi + b_5\lambda h + b_6\varphi h \\ + b_7\lambda^2 + b_8\varphi^2 + b_9h^2 + \varepsilon \tag{3}$$

where $b_0 - b_9$ are the coefficients to be determined.

To evaluate the quality of interpolation, errors are calculated by the cross-validation method. The functions are:

$$ME = \frac{1}{n}\sum_{i=1}^{n}(y_i - x_i) \tag{4}$$

$$MABE = \frac{1}{n}\sum_{i=1}^{n}\frac{|y_i - x_i|}{x_i} \tag{5}$$

where ME is mean error; MABE is relative error; n is the number of stations; y_i is the predicted value at the ith station and x_i is the observed value at the ith station.

The central longitude and latitude of the Taoer river basin are 121.949°E and 46.12°N, respectively. Longitude/latitude ($\triangle\lambda/\triangle\varphi$) of the basin is standardized by subtracting the central longitude/latitude. Models between macro-geographical factors and meteorological variables are established by step regression in SPSS (Statistical Package for the Social Sciences) 13.0. To obtain a grid map of meteorological variables, the models are performed with the AML (ArcInfo Macro Language) module in ArcGIS 8.3.

Spatial modelling of the radiation environment

The radiation measurements are too limited to be interpolated in the study area. In this study, the radiation environment was therefore spatially modelled based on longitude, latitude, elevation, slope and aspect in order to reflect topographic influences. Surface net radiation (R_n) is the balance of the incoming and outgoing shortwave and longwave radiation components of the Earth's surface, or the balance of net solar radiation and net longwave radiation at the surface, and is used for the increase of temperature change and evapotranspiration.

There are three approaches for obtaining surface net radiation:

1. Use the radiation balance model, which is given as RB = $G(1 - RS) + (LD - LU)$, where RB is the radiation balance of the surface, G is the global radiation, RS is the surface albedo, LD is the longwave radiation
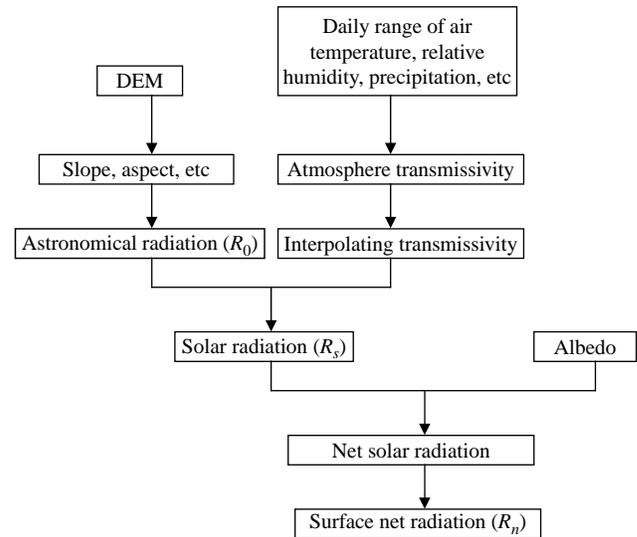

Figure 5 | Technique routine for surface net radiation calculation.

reaching the surface and LU is the longwave radiation emitted by the surface (e.g. Rimóczi-Paál 2005).

2. Obtain net radiation from a joint product from NCEP (the National Centers for Environmental Prediction) and NCAR (the National Center for Atmospheric Research) (Jenne 1992; Yu *et al.* 2004).

3. Use methods such as the Chang Jen-Hu (Chang 1970) and those used for Penman equation and Penman–Monteith equation.

In particular, the Chang Jen-Hu equation was modified by recalculating its four coefficients with surface net radiation at 50 stations in China (Yu *et al.* 2004). The modified Chang Jen-Hu Equation (Equation (21)) was selected in our study to calculate surface net radiation due to the better results in China (Yu *et al.* 2004; Liu *et al.* 2006).

Taking daily surface net radiation for the 15th day of the month as mean daily value of the month, Figure 5 depicts the technique.

Astronomical radiation

The astronomical radiation on a slope during a period of sunshine is expressed as:

$$R_0 = \frac{T}{2\pi}\left(\frac{1}{\rho}\right)^2 I_0[u\sin\delta(\omega_{ss} - \omega_{sr}) + v\cos\delta(\sin\omega_{ss} - \sin\omega_{sr}) \\ - w\cos\delta(\cos\omega_{ss} - \cos\omega_{sr})] \tag{6}$$

where R_0 is astronomical radiation $(\mathrm{MJ\,m^{-2}})$; T is the length of a day $(1{,}440\,\mathrm{min})$; $(1/\rho)^2$ is the Earth–Sun distance factor; I_0 is the solar constant $(0.082\,\mathrm{MJ\,m^{-2}\,min^{-1}})$; ω_{sr}, ω_{ss} are initial and terminal hour angles of sunshine period respectively; u, v and w are factors related to geography and topography and are defined as:

$$u = \sin\varphi\cos\alpha - \cos\varphi\sin\alpha\cos\beta \tag{7}$$

$$v = \sin\varphi\sin\alpha\cos\beta + \cos\varphi\cos\alpha \tag{8}$$

$$w = \sin\alpha\sin\beta \tag{9}$$

where φ is latitude, α is slope and β is aspect (in radians).

Solar declination and the Earth–Sun distance factor are calculated by the Fourier series (Zuo *et al.* 1991):

$$\delta = 0.006894 - 0.399512\cos\tau + 0.072075\sin\tau$$
$$- 0.006799\cos 2\tau + 0.000896\sin 2\tau$$
$$- 0.002689\cos 3\tau + 0.001516\sin 3\tau \tag{10}$$

$$\left(\frac{1}{\rho}\right)^2 = 1.000109 + 0.033494\cos\tau + 0.001472\sin\tau$$
$$+ 0.000768\cos 2\tau + 0.000079\sin 2\tau \tag{11}$$

where τ is hour angle (radians), defined $\tau = 2\pi(D_n - 1)/365$, and D_n is day number (between 1 and 365).

The sunrise $(-\omega)$ and sunset (ω) hour angles only relate to latitude and solar declination. It is expressed as:

$$\omega = \arccos(-\tan\phi\tan\delta) \tag{12}$$

The sunshine period in a day is divided into 10 sub-periods with a time-step of $1/5\omega$, i.e. 25–46 min in this study. The daily value comprises the accumulative radiation of 10 sub-periods.

Atmospheric transmissivity

Atmospheric transmissivity is the ratio of solar radiation to astronomical radiation, which reflects the weakening effect of atmosphere on solar radiation. It can be expressed as:

$$t = t_{\max}\, t_f\, \mathrm{rain} \tag{13}$$

$$t_{\max} = \frac{\sum_{s=sr}^{ss} Q_{\mathrm{spot\cdot s}} \cdot t_{0\cdot\mathrm{nadis\cdot dry}}^{(P_Z/P_0)\cdot m_\theta}}{\sum_{s=sr}^{ss} Q_{\mathrm{spot\cdot s}}} + 0.001\alpha e \tag{14}$$

$$t_f = 1.0 - 0.9\exp(-B\Delta T^C) \tag{15}$$

$$B = a + 0.001be \tag{16}$$

where t is actual transmissivity; $t_{\max}$ is clear-sky transmissivity (related to the number of days in a year, vapour pressure, geographical position and elevation); t_f is correction coefficient; Q_{spots} is astronomical radiation at the time of s; sr and ss are time of sunrise and sunset; $t_{0\mathrm{nadisdry}}$ is dry atmospheric transmissivity on sea level at noon; P_z and P_0 are air pressure at height z and sea level, respectively; m_θ is optical air mass when solar zenith is θ; α is a coefficient affected by water vapour; e is vapour pressure (k Pa); B and C are empirical coefficients; ΔT is daily range of air temperature; and rain is a coefficient affected by precipitation. The value of rain is normally 0.75–0.8 on rainy or snowy days, otherwise 1 (He *et al.* 2004). In our study, rain is set to 0.8 on rainy or snowy days and 1 on clear days. According to the proportion of rainy/snowy days to all days in a month at Taonan station in the study area, the mean monthly value of rain is 0.906–0.993. Here, values of main parameters are: $t_{0\mathrm{nadisdry}} = 0.87$; $\alpha = -0.000061$; $a = 0.0173$; $b = 0.0000122$; $C = 1.5$ (Glassy & Running 1994; Li *et al.* 2003; He *et al.* 2004). Atmospheric transmissivity t is interpolated by inverse distance weighting method to obtain a grid map.

The correction coefficient of air pressure is defined as:

$$\frac{P_Z}{P_0} = [(288 - 0.0065h)/288]^{5.256} \tag{17}$$

where h is height above the ground (m).

Air mass at sea level is defined as:

$$M_0 = [1299 + (614\sin\alpha)^2]^{0.5} - 614\sin\alpha \tag{18}$$

$$\sin\alpha = \sin\varphi\sin\delta + \cos\varphi\cos\delta\cos\omega \tag{19}$$

Solar radiation is defined as:

$$R_s = R_0 t \tag{20}$$

Surface net radiation

The modified Chang Jen-Hu method calculates monthly surface net radiation with mean air temperature, vapour

pressure and solar radiation (Yu *et al.* 2004):

$$R_n = (1 - \rho)R_s - \sigma T^4 (a + bt - c\sqrt{0.1 \cdot e} - dt\sqrt{0.1 \cdot e}) \qquad (21)$$

where R_n is monthly surface net radiation (MJ m^{-2}); ρ is albedo (0.23); R_s is solar radiation (MJ m^{-2}); σ is Stefan-Boltzmann constant (4.903×10^{-9} MJ K^{-4} m^{-2}); T is temperature (K); t is atmospheric transmissivity; e is vapour pressure (k Pa); a, b, c and d are empirical coefficients and are kept constant throughout the 12 months of a year in the original functions. In this study, the coefficients vary in different months and were calculated with surface net radiation at 50 stations in China by Yu *et al.* (2004).

Calculating ET$_0$

Based on grid maps of the required meteorological variables and radiation, ET$_0$ is calculated by the Penman–Monteith (P–M) method. This was recommended by the FAO as the standard method to calculate ET$_0$ and has been used worldwide (Allen *et al.* 1998):

$$ET_0 = \frac{0.408\Delta(R_n - G) + \gamma \frac{900}{T+273} u_2 (e_s - e_a)}{\Delta + \gamma(1 + 0.34u_2)} \qquad (22)$$

where ET$_0$ is the reference evapotranspiration (mm d^{-1}); R_n is the net radiation at the crop surface (MJ m^{-2} d^{-1}); G is the soil heat flux (MJ m^{-2} d^{-1}) (neglected for daily calculation since the magnitude of the flux in this case is relatively small); T is the mean daily air temperature at 2 m height (°C); u_2 is the wind speed at 2 m height (m s^{-1}); e_s is the saturation vapour pressure (kPa); e_a is the actual vapour pressure (kPa); $e_s - e_a$ is the saturation vapour pressure deficit (kPa); Δ is the slope of the saturated water–vapour pressure curve (kPa/°C); and γ is the psychrometric constant (kPa/°C). The computation of all data required for the calculation of ET$_0$ followed the method and

procedure given in Chapter 3 of the FAO paper 56 (Allen *et al.* 1998). If the data time-step is monthly then the resultant ET$_0$ is provided with units of mm month^{-1} (Allen *et al.* 1998; McVicar *et al.* 2007).

RESULTS AND DISCUSSION

Spatially interpolating wind speed

The interpolation quality for wind speed by the IDW method was evaluated in Table 2. Mean errors are all positive, which indicates that predicted values are higher than observed values. Mean errors in January, February and December are larger than the standard deviation, so we can conclude that the quality of spatial interpolation of wind speed is lowest in winter. The average of relative error is 8.8%. Errors are lower from April to October with relative error <10% and higher in other months.

Through inverse distance weighting interpolation, 12 grid maps of mean wind speed in different months are obtained. Taking, for example, January and July (Figure 6), wind speed in January was generally high and decreased gradually from the south to the north with maximum value in Tuquan. On the other hand, wind speed in July was generally low and decreased from the southeast to the northwest with the lowest value in Suolun. Spatial variation in January was larger than in July for wind speed.

Spatially interpolating relative humidity and air temperature

The results of spatially modelling relative humidity are shown in Table 3. It can be seen that all factors selected by stepwise regression are at significant level $\alpha = 0.05$ and most models were established with two factors. Multiple correlation coefficients in every month except for March all

Table 2 | Error of mean wind speed interpolation by IDW method and the mean and standard deviation of wind speed during recent 45 years in the Taoer river basin

	Jan	Feb	Mar	Apr	May	Jun	Jul	Aug	Sep	Oct	Nov	Dec
Mean error (m s^{-1})	0.40	0.35	0.32	0.24	0.16	0.09	0.08	0.10	0.18	0.23	0.27	0.34
Relative error (%)	16.6	13.6	10.2	6.8	4.8	3.6	3.8	5.0	7.8	8.5	10.2	14.3
Mean (m s^{-1})	2.42	2.58	3.10	3.54	3.28	2.55	2.12	1.97	2.34	2.67	2.62	2.40
Standard deviation	0.37	0.31	0.36	0.39	0.42	0.29	0.24	0.25	0.29	0.29	0.34	0.30
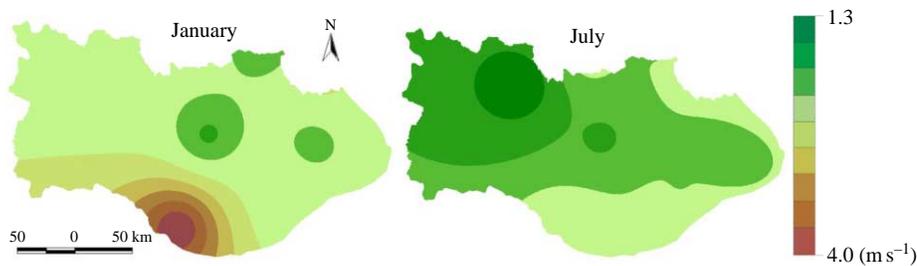
Figure 6 | Spatial distribution of mean wind speed in January and July averaged over 1961–2005 for the Taoer river basin (m s⁻¹).

Table 3 | Models between macro-geographical factors and relative humidity in the Taoer river basin. The parameters $\triangle \lambda$ and $\triangle \varphi$ are the standardized longitude and latitude obtained by subtracting the central longitude and latitude, respectively. The parameter h is elevation
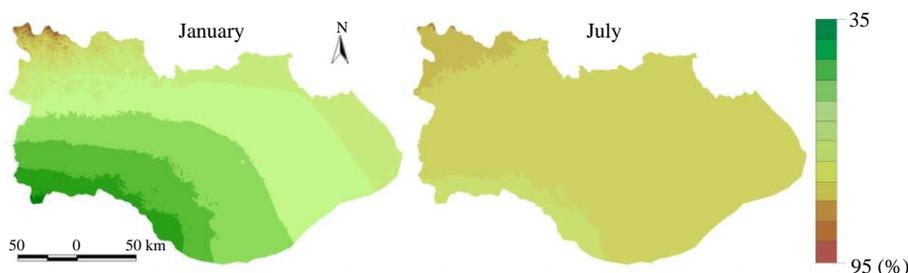
	Model	Multiple correlation coefficient R	Variance ratio F	Number of factors in the model	Relative error (%)
Jan	$55.231 + 1.028\triangle\varphi\triangle\varphi + 0.026\triangle\varphi h + 4.226\triangle\lambda$	0.973	65.4	3	2.8
Feb	$48.192 + 0.018\triangle\varphi\, h + 2.709\triangle\varphi\triangle\varphi$	0.964	78.0	2	9.8
Mar	$40.744 + 0.0000246hh$	0.833	29.4	1	7.7
Apr	$37.485 + 0.009\triangle\varphi h + 1.896\triangle\varphi\triangle\varphi$	0.949	54.0	2	8.4
May	$40.185 + 0.003\triangle\varphi h + 1.662\triangle\varphi\triangle\varphi$	0.917	31.5	2	6.3
Jun	$58.651 + 0.007\triangle\varphi h - 1.554\triangle\lambda\triangle\varphi$	0.926	36.3	2	1.3
Jul	$72.138 + 0.389\triangle\lambda - 1.070\triangle\lambda\triangle\varphi + 0.005\triangle\varphi h$	0.899	15.4	3	0.4
Aug	$72.02 + 0.005\triangle\varphi h - 1.513\triangle\lambda\triangle\varphi$	0.919	32.8	2	0.6
Sep	$60.989 + 0.005\triangle\varphi h + 1.248\triangle\varphi\triangle\varphi$	0.900	25.7	2	4.2
Oct	$51.000 - 2.053\triangle\lambda\triangle\varphi + 0.005\triangle\varphi h + 1.186\triangle\varphi\triangle\varphi$	0.946	31.4	3	6.1
Nov	$52.607 + 0.011\triangle\varphi h + 2.217\triangle\varphi\triangle\varphi$	0.932	39.9	2	8.5
Dec	$57.676 + 4.489\triangle\lambda + 0.027\triangle\varphi h$	0.946	50.9	2	5.5

exceed 0.90 at significant level $\alpha = 0.01$. Relative errors are all under 10% with an average of 5.1% (<5% during June to September).

Standard longitude grid map, standard latitude grid map and elevation grid map were employed in ArcGIS to create a monthly relative humidity grid map with the appropriate model and 12 maps were obtained. Considering January and July (Figure 7), patterns of relative humidity in

difference months are similar, with values decreasing gradually from the south to the north in the upper reach (location of highest elevation). In the middle and lower reaches, its spatial variation is small and distribution is homogeneous (particularly in July). The spatial variation of relative humidity was larger in January than in July.

Models to spatially simulate air temperature are listed in Table 4. All factors selected by stepwise regression except

Figure 7 | Spatial distribution of mean relative humidity in January and July averaged over 1961–2005 for the Taoer river basin (%).

Table 4 | Models between macro-geographical factors and mean air temperature in the Taoer river basin (parameters as for Table 3)

	Model	Multiple correlation coefficient R	Variance ratio F	Number of factors in the model	Relative error (%)
Jan	$-15.848 - 0.008\triangle\varphi h - 0.495\triangle\varphi\triangle\varphi$	0.930	148.3	2	5.2
Feb	$-11.646 - 0.011\triangle\varphi h + 1.284\triangle\varphi - 0.231\triangle\varphi\triangle\varphi$	0.934	317.2	3	3.2
Mar	$-2.782 - 0.0000049hh - 0.003\triangle\varphi h$ $+0.256\triangle\lambda\triangle\varphi + 0.158\triangle\lambda\triangle\lambda - 0.001h$	0.939	452.5	5	5.7
Apr	$7.991 - 0.004\triangle\varphi h - 0.004h$	0.936	718.2	2	2.7
May	$16.998 - 0.002\triangle\varphi h - 0.007h - 0.316\triangle\lambda$	0.938	1134.1	3	0.6
Jun	$21.806 - 0.006h - 0.002\triangle\varphi h$	0.933	421.0	2	0.6
Jul	$24.389 - 0.007h - 0.501\triangle\varphi$	0.933	401.2	2	0.8
Aug	$22.559 - 0.007h - 0.618\triangle\varphi$	0.921	319.3	2	0.9
Sep	$15.984 - 0.007h - 0.878\triangle\varphi + 0.241\triangle\lambda\triangle\varphi$	0.934	326.6	3	0.9
Oct	$6.546 - 0.004\triangle\varphi h - 0.004h$	0.937	928.8	2	0.8
Nov	$-5.498 - 0.007\triangle\varphi h - 0.0000011hh + 0.284\triangle\varphi$	0.934	330.3	3	3.9
Dec	$-13.548 - 0.007\triangle\varphi h - 0.333\triangle\varphi\triangle\varphi$	0.926	206.5	2	3.8

for March are at significance level $\alpha = 0.05$ and most models were established with two factors. In order to decrease relative error in March, significance level was modified to $\alpha = 0.2$ and the selected factors amounting to 5. Multiple correlation coefficients all exceed 0.98 at significance level $\alpha = 0.01$. Relative errors are all under 6% with the average of 2.4 (<1% during May to October).

Like relative humidity, 12 grid maps of air temperature in different months are obtained. Considering January and July (Figure 8), air temperature decreased gradually from the southeast to the northwest through the whole basin. The air temperature distribution in the middle and lower reaches, mainly governed by latitude, was homogenous. The air temperature in the mountainous upper reach showed obvious topographic influence. Air temperature showed the same seasonal pattern as relative humidity.

Spatially modelling the radiation environment

We obtained 12 grid maps on net surface radiation; those for January and July are depicted in Figure 9. We found less spatial variation in January than in July. The distribution of radiation was affected by topography (elevation, slope and aspect) in the study area. Radiation was higher in the low elevation and low latitude area in the south and east of the basin. Net surface radiation was generally high in July and showed high homogenous distribution in the plain in the middle and lower reach.
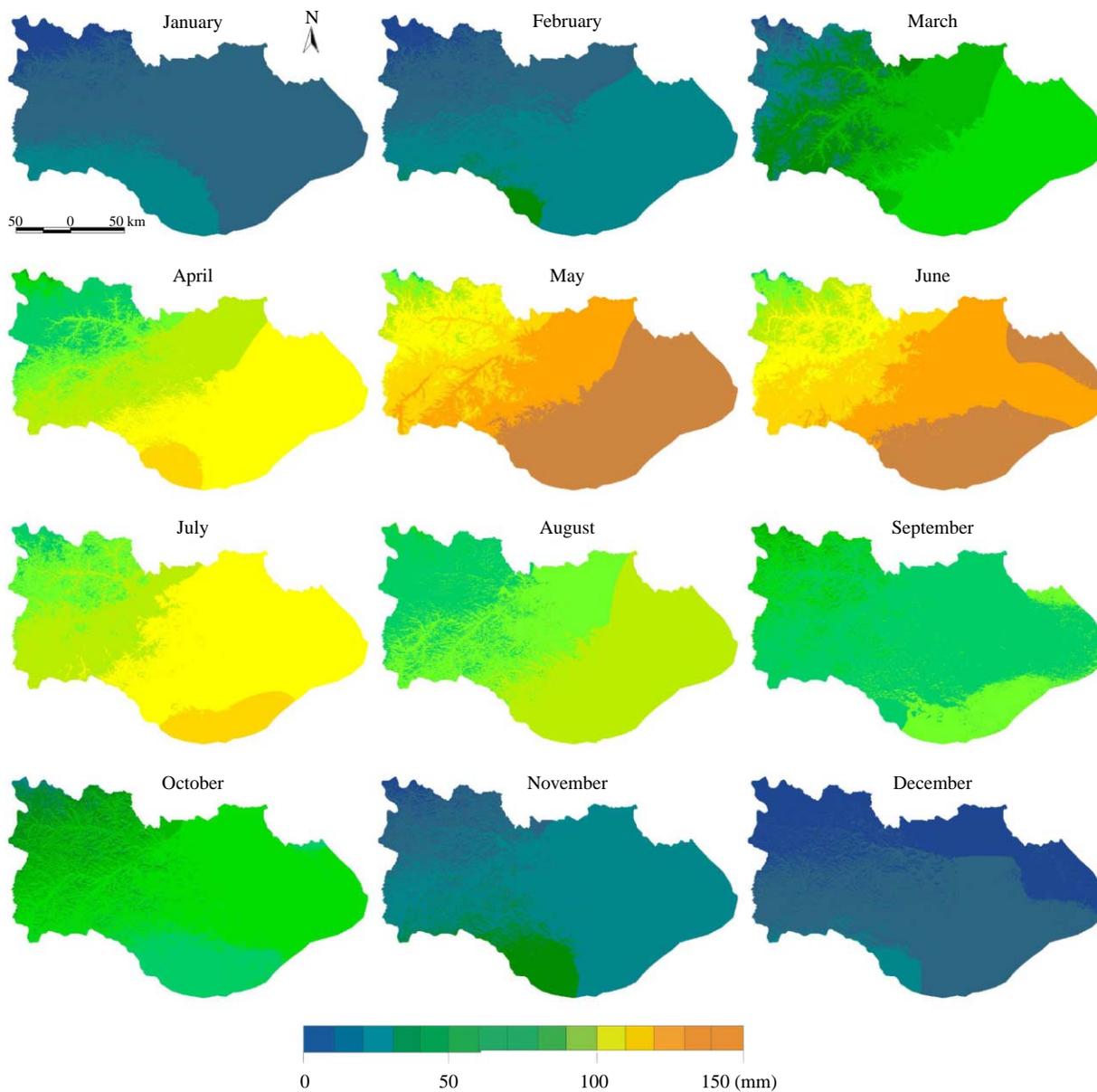
Spatial variation of ET$_0$

Using grid maps of climate variables and net surface radiation, ET$_0$ was calculated by the Penman–Monteith equation at each grid cell at the high resolution of 200 m.
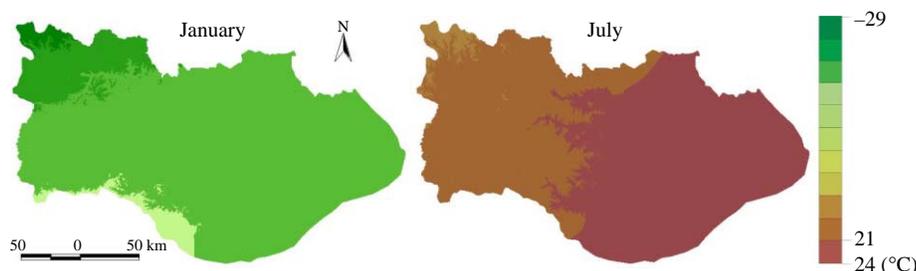
Figure 8 | Spatial distribution of mean air temperature in January and July averaged over 1961–2005 for the Taoer river basin (℃).
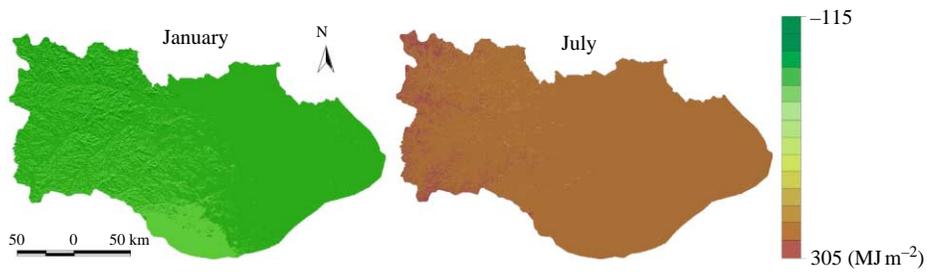
Figure 9 │ Spatial distribution of mean surface net radiation in January and July averaged over 1961–2005 for the Taoer river basin (MJ m^{-2}).

Figure 10 │ Spatial distribution of monthly ET$_0$ considering topographic influences averaged over 1961–2005 for the Taoer river basin (mm).

Table 5 │ Comparison of errors of ET_0 interpolation by tri-variate secondary trend surface, IDW, kriging (linear) and kriging (exponential) (values in this table are mean relative errors of 12 months from the cross-validation tests)

	Interpolate-then-calculate	Calculate-then-interpolate			
	Tri-variate secondary trend surface	Tri-variate secondary trend surface	IDW	Kriging (linear)	Kriging (exponential)
Relative error (%)	8.4	10.8	15.8	11.2	13.1

Figure 10 shows monthly ET_0 grid maps from January to December averaged over the 45 years. It can be seen that the spatial variation of ET_0 in winter was less than that in the other seasons. In the plains adjacent to the lower reach of the Taoer river, ET_0 demonstrated a homogenous distribution. In mountainous regions in the upper reach, low ET_0 are measured in the ridges while high ET_0 is measured in the valleys and plains. Generally, low ET_0 were found in the southern Great Xingan mountains. For the monthly ET_0 spatial distributions from March to September, ET_0 decreased from the southeast to the northwest. In the other months, high values were found in the south and ET_0 decreased from the south to the north. The magnitude of ET_0 in difference months highlighted the monthly variation with a maximum in May and low values in winter.

Comparison of spatial interpolation methods for ET_0

The spatial distributions of monthly ET_0 by 'calculate-then-interpolate' method were interpolated by tri-variate secondary trend surface method and the three interpolation methods which performed best: IDW, kriging (linear) and kriging (exponential). The relative error of interpolation is lowest for tri-variate secondary trend surface method with a value of 10.8% (Table 5).

The spatial distribution of ET_0 by IDW and ordinary kriging methods only consider the effects of distance between sample points and interpolated points, and do not take into account the effects of elevation variation. These methods would provide accurate results when the number of sample points is large with uniform geographical conditions, e.g. ET_0 interpolation in Greece (Dalezios *et al.* 2002) and Changjiang catchment (Xu *et al.* 2006), and precipitation interpolation in the Yellow river basin (Liu *et al.* 2008).

ET_0 is influenced by meteorological variables which vary with elevation, slope and aspect (Tong *et al.* 2007). The reason for the unsatisfactory results with the 'calculate-then-interpolate' method is that the elevation varies considerably over the basin, and the number of sample points is also limited. The spatial distribution of ET_0 by tri-variate secondary trend surface which considered the DEM better reflected the effects of topography on ET_0 and is more realistic compared to the other three methods.

The relative error of ET_0 distribution by tri-variate secondary trend surface for the 'interpolate-then-calculate' method is 8.4% (Table 5), which is lower than that by tri-variate secondary trend surface for the 'calculate-then-interpolate' method (10.8%). Topography was seen to affect values of ET_0 due to the influence of elevation, slope and aspect on meteorological variables during processes to obtain ET_0 distribution. The comparison indicated that the 'interpolate-then-calculate' method better reflected the effects of topography on ET_0 than the 'calculate-then-interpolate' method.

CONCLUSIONS

In this paper, the 'interpolate-then-calculate' approach was implemented to calculate ET_0 at each grid cell to obtain a high-resolution surface of long-term averaged monthly ET_0. This approach exhibits topographic influences on the forcing climate variables and net radiation by spatially interpolating wind speed (considering longitude and latitude), relative humidity and air temperature (considering elevation, longitude and latitude) and spatially modelling net surface radiation environment (considering slope, aspect, elevation, longitude and latitude) with 200 m resolution.

The 'interpolate-then-calculate' approach is superior to a geometric dimensional 'calculate-then-interpolate' approach, which would only have used 15 points in and around the Taoer river basin. In an area with complex topography and a small number of stations, the 'interpolate-then-calculate' approach which considers the DEM should therefore be preferred to the 'calculate-then-interpolate' approach. This study also presented the spatial distribution

of ET_0 averaged over the past 45 years, which is valuable information for irrigation and water resources management in the Taoer river basin.

The conclusions of this study are as follows.

1. On comparing 11 interpolation methods, IDW method was found most suitable for interpolating wind speed. Tri-variate secondary trend surface method was best for interpolating mean air temperature and relative humidity, since it takes the DEM into account.
2. In order to adequately reflect topographic influences, the radiation environment was modelled considering slope and aspect in addition to longitude, latitude and elevation. This result better reflected the topographic influence than that by ANUSPLIN software by McVicar *et al.* (2007) which only considering longitude, latitude and elevation.
3. The three meteorological variables and radiation showed strong seasonal variation. Spatial variations of the three meteorological variables in January were larger than that in July, while net surface radiation showed the opposite.
4. The resulting ET_0 calculated at each grid cell at 200 m resolution showed strong seasonal and spatial variation. Low ET_0 was found in the southern Great Xingan mountains in the upper basin.
5. The 'interpolate-then-calculate' approach showed better interpolation quality results than the 'calculate-then-interpolate' approach for calculating ET_0.

ACKNOWLEDGEMENTS

REFERENCES

Allen, R. G., Pereira, L. S., Raes, D. & Smith, M. 1998 Crop evapotranspiration: guidelines for computing crop water requirements. *FAO Irrigation and Drainage Paper 56*, Rome, Italy.

Blackie, J. R. & Simpson, T. K. M. 1993 Climatic variability within the Balquhidder catchments and its effect on Penman potential evaporation. *J. Hydrol.* **145**, 371–387.

Chang, J. H. 1970 Global distribution of net radiation according to a new formula. *Ann. Assoc. Am. Geogr.* **60**, 340–351.

Dalezios, N. R., Athanasios, L. & Bampzelis, D. 2002 Spatial variability of reference evapotranspiration in Greece. *Phys. Chem. Earth* **27**, 1031–1038.

Daly, C. 2006 Guidelines for assessing the suitability of spatial climate data sets. *Int. J. Climatol.* **26**, 707–721.

DehghaniSanij, H., Yamamotoa, T. & Rasiah, V. 2004 Assessment of evapotranspiration estimation models for use in semi-arid environments. *Agric. Water Manage.* **64**, 91–106.

Dinpashoh, Y. 2006 Study of reference crop evapotranspiration in I. R. of Iran. *Agric. Water Manage.* **84**, 123–129.

Donohue, R. J., Roderick, M. L. & McVicar, T. R. 2007 On the importance of including vegetation dynamics in Budyko's hydrological model. *Hydrol. Earth Syst. Sci.* **11**, 983–995.

Franke, R. 1982 Scattered data interpolation: tests of some methods. *Math. Comput.* **38**(157), 181–200.

Gao, Q., Yu, M. & Yang, X. S. 2000 An analysis of sensitivity of terrestrial ecosystems in China to climate change using spatial simulation. *Clim. Change* **47**, 373–400.

Glassy, J. M. & Running, S. W. 1994 Validating diurnal climatology logic of the MT-CLIM model across a climatic gradient in Oregon. *Ecol. Appl.* **4**, 248–257.

He, H. L., Yu, G. R., Liu, X. A., Su, W., Niu, D. & Yue, Y. Z. 2004 Study on spatialization technology of terrestrial eco–information in China (II): solar radiation. *J. Nat. Resour.* **19**, 679–687 (in Chinese with English abstract).

Huntington, T. G. 2006 Evidence for intensification of the global water cycle: review and synthesis. *J. Hydrol.* **319**, 83–95.

Hutchinson, M. F. 2004 *ANUSPLIN Version 4.3 User Guide.* http://cres.anu.edu.au/outputs/software.php

Hutchinson, M. F., Kalma, J. D. & Johnson, M. E. 1984 Monthly estimates of wind speed and wind run for Australia. *J. Climatol.* **4**, 311–324.

Jeffrey, S. J., Carter, J. O., Moodie, K. B. & Beswick, A. R. 2001 Using spatial interpolation to construct a comprehensive archive of Australian climate data. *Environ. Modell. Softw.* **16**, 309–330.

Jenne, R. L. 1992 *Data for Reanalysis–Inventories.* National Center for Atmospheric Research, Boulder, Colorado, US.

Jiang, D. J. 2007 Influence of climate change and land use/land cover change on runoff in the middle and upper reaches of Tao'erhe river Basin. PhD Thesis. Institute of Geographic Sciences and Natural Resources Research, Chinese Academy of Sciences (in Chinese with English abstract).

Joshua, B. F., Terry, A. D. & Ye, Q. 2005 Evapotranspiration models compared on a Sierra Nevada forest ecosystem. *Environ. Modell. Softw.* **20**, 783–796.

Krajewski, W. F. 1987 Cokriging radar-rainfall and rain gage data. *J. Geophys. Res.* **92**(8), 9571–9580.

Li, H. T., Xia, J., Shen, W. Q., Liu, Q. J. & Yu, G. R. 2003 Improving the estimation of solar radiation of mountain microclimate simulation model in subtropical mountainous region of China. *J. Mountain Sci.* **21**(5), 542–551 (in Chinese with English abstract).

Liang, L. Q., Li, L. J., Zhang, L., Li, J. Y. & Li, B. 2008 Sensitivity of the Penman-Monteith reference crop evapotranspiration in the Taoer river basin. *Chin. Geogr. Sci.* **18**(4), 340–347.

Liu, X. Y. & Lin, E. D. 2005 Performance of the Priestley-Taylor equation in the semiarid climate of North China. *Agric. Water Manage.* **71**, 1–17.

Liu, X. A., Yu, G. R., He, H. L., Cai, F. & Zhu, Q. L. 2006 Research on the calculating of surface net radiation in China. *J. Nat. Resour.* **21**(1), 139–145.

Liu, Q., Yang, Z. F. & Cui, B. S. 2008 Spatial and temporal variability of annual precipitation during 1961–2006 in Yellow river basin. *China. J. Hydrol.* **361**, 330–338.

Marquínez, J., Lastra, J. & García, P. 2003 Estimation Models for precipitation in Mountainous regions: the use of GIS and multi-variate analysis. *J. Hydrol.* **270**, 1–11.

McVicar, T. R. & Jupp, D. L. B. 2002 Using covariates to spatially interpolate moisture availability in the Murray-Darling basin: a novel use of remotely sensed data. *Remote Sens. Environ.* **79**, 199–212.

McVicar, T. R., Zhang, G., Bradford, A. S., Wang, H., Dawes, W. R., Zhang, L. & Li, L. T. 2002 Monitoring regional agricultural water use efficiency for Hebei Province on the North China Plain. *Aust. J. Agric. Res.* **53**, 55–76.

McVicar, T. R., Van Niel, T. G., Li, L. T., Hutchinson, M. F., Mu, X. M. & Liu, Z. H. 2007 Spatially distributing monthly reference evapotranspiration and pan evaporation considering topographic influences. *J. Hydrol.* **338**, 196–220.

Price, D. T., McKenny, D. W., Nalder, I. A., Hutchinson, M. F. & Kesteven, J. L. 2000 A comparison of two statistical methods for spatial interpolation of Canadian monthly mean climate data. *Agric. For. Meteorol.* **101**, 81–94.

Rimóczi-Paál, A. 2005 Mapping of radiation balance components for region of Hungary using satellite information. *Phys. Chem. Earth* **30**, 151–158.

Stahl, K., Moore, R. D., Floyer, J. A., Asplin, M. G. & McKendry, I. G. 2006 Comparison of approaches for spatial interpolation of daily air temperature in a large region with complex topography and highly variable station density. *Agric. For. Meteorol.* **139**, 224–236.

Tong, L., Kang, S. Z. & Zhang, L. 2007 Temporal and spatial variations of evapotranspiration for spring wheat in the Shiyang river basin in northwest China. *Agric. Water Manage.* **87**, 241–250.

Utset, A., Farré, I. & Martínez-Cob, A. 2004 Comparing Penman-Monteith and Priestley-Taylor approaches as reference evapotranspiration inputs for modelling maize water-use under Mediterranean conditions. *Agric. Water Manage.* **66**, 205–219.

Vicente-Serrano, S. M., Saz-Sanchez, M. A. & Cuafrat, J. M. 2003 Comparative analysis of interpolation methods in the middle Ebro valley (Spain): application to annual precipitation and temperature. *Clim. Res.* **24**(2), 161–180.

Watson, D. F. & Philip, G. M. 1985 A refinement of inverse distance weighted interpolation. *Geo-Processing* **2**(4), 315–327.

Xu, C. Y., Gong, L. B., Jiang, T., Chen, D. L. & Sing, V. P. 2006 Analysis of spatial distribution and temporal trend of reference evapotranspiration and pan evaporation in Changjiang (Yangtze river) catchment. *J. Hydrol.* **327**, 81–93.

Yan, H., Nix, H. A., Hutchinson, M. F. & Booth, T. H. 2005 Spatial interpolation of monthly mean climate data for China. *Int. J. Climatol.* **25**, 1369–1379.

Yates, S. R. & Warrick, A. W. 1987 Estimating soil water using Cokriging. *Soil Sci. Soc. Am. J.* **51**(1), 23–30.

Yoshino, M. M. 1975 *Climate in a Small Area: An Introduction to Local Meteorology*. University of Tokyo Press, Tokyo.

Yu, G. R., He, H. L. & Liu, X. A. 2004 *Atlas for Spatialized Information of Terrestrial Ecosystem in China: Volume of Climatological Elements*. China Meteorological Press, Beijing, China (in Chinese).

Zhang, D. F. & Wang, S. J. 2002 Study on the eco-geo-environment of land salionization in west Jilin Province. *Chin. J. Soil Sci.* **33**, 90–93 (in Chinese with English abstract).

Zhang, F. M. & Shen, S. H. 2007 Spatial distribution and temporal trend of reference crop evapotranspiration in China. *J. Nanjing Inst. Meteorol.* **30**(5), 705–709 (in Chinese with English abstract).

Zhang, L., Dawes, W. R. & Walker, G. R. 2001 Response of mean annual evapotranspiration to vegetation changes at catchment scale. *Water Resour. Res.* **37**, 701–708.

Zhao, Y. L. 1999 *Distribution of Fragile Types of Eco-Environment and Their Comprehensive Management in China*. Beijing: China Environmental Science Press (in Chinese).

Zhao, C. Y., Nan, Z. R. & Feng, Z. D. 2004 GIS-assisted spatially distributed modelling of the potential evapotranspiration in semi-arid climate of the Chinese Loess Plateau. *J. Arid Environ.* **58**, 387–403.

Zuo, D. K., Zhou, Y. H. & Xiang, Y. Q. 1991 *Research on Radiation at Earth Surface*. Science Press, Beijing, China (in Chinese).